Supporting information for

P-block tin single atom catalyst for improved electrochemistry in lithium-sulfur battery: a theoretical and experimental study

Experimental Section

Materials: In this study, trisodium citrate dihydrate (AR) was purchased from Sinopharm Chemical Reagent Co., Ltd. (Shanghai, China). $SnCl_2$ (99%) were purchased from Rhawn (Tianjin, China). Dicyandiamide (AR) was purchased from Macklin (Shanghai, China). HCl (AR) was purchased from Rionlon (Tianjin, China). Sulfur (99.95%) was purchased from Aladdin (Shanghai, China). Ethanol (AR) was purchased from Yuanli company (Tianjin, China). Lithium sulfide (99.9%) was purchased from Heowns (Tianjin, China). All chemicals were used without further purification.

1. Methods

Synthesis of carbon nanosheets: Carbon nanosheet substrates were prepared by directly pyrolyzing trisodium citrate dehydrate in inert atmosphere. In detail, 6 g trisodium citrate dehydrate was placed into ceramic crucible uniformly and calcined at 700 °C for 1 h under Ar atmosphere with a heating rate of 5 °C min^{-1}. The product was further washed with 80 °C deionized water and ethanol for 3 times and dried at 60 °C for 24 h to obtain the carbon nanosheets.

Synthesis of Sn$_{SA}$-NC and NC: 60 mg as-prepared carbon nanosheets, 38 mg $SnCl_2$ and 563 mg dicyandiamide were dispersed into 40 mL ethanol and stirred overnight at room temperature. The solution was under continuously stirring at 70 °C until the solvent completely evaporated. The obtained powders were uniformly grinded by a mortar and pestle. Subsequently, the powder was annealed at 700 °C for 2 h under Ar atmosphere with a heat rate of 5 °C min^{-1}, followed by etching in 4 M HCl at 80 °C for 24 h. Sn$_{SA}$-NC was obtained after washing with a large amount of

deionized water and dried at 60 °C overnight. NC was prepared by a similar route without the addition of $SnCl_2$.

Synthesis of S/C composite: The S/C composite was prepared by a melt-diffusion method. The sulfur and carbon black (super P) were mixed with a ratio of 2:1 and grinded evenly. The mixture was sealed in a vacuum glass and heated at 155 °C for 12 h.

2. Materials characterization

The microstructures and surface morphologies were obtained by using atomic force microscope (AFM, CSPM5500), thermal field emission scanning electron microscope (SEM, JSM-7800F, JEOL) and transmission electron microscopy (TEM, JEM-2100F, JEOL). STEM and EDS mapping images were taken using STEM (EM-24560) and EDS (Oxford). HADDF-AC-STEM images were captured by special aberration corrected transmission electron microscope (AC-TEM, JEM-ARM200F, JEOL). X-ray diffraction (XRD, D8 Advance, Bruker) patterns were collected with Cu Kα radiation ($\lambda = 1.54056$ Å) at 40 kV and 40 mA. The chemical and electronic state of the surface was measured by X-ray photoelectron spectroscopy (XPS, Axis Supra, Kratos). The N_2 adsorption-desorption isotherms measurement (Autosorb iQ) was employed at liquid-nitrogen temperature (78 K) to analyze the specific surface area and the pore size distribution based on multipoint Brunauer-Emmett-Teller (BET) theory. The metal content was measured by Inductively Coupled Plasma Mass Spectrometry (ICP-MS, Agilent 7700x). The adsorption spectra of 5 mM Li_2S_8 in 1,3-dioxolane (DOL) and 1,2-dimethoxyethane (DME) (1:1, v/v) solution were carried out via ultraviolet-visible (UV-vis) spectrophotometer (UV-2700). The sulfur content of cathode was calculated according to the thermogravimetric analysis (TGA, STA 449 C, NETZSCH) carried out under N_2 flow with a heating rate of 10 °C min^{-1}.

The X-ray absorption find structure spectra Sn K-edge were collected at BL14W1 beamline of Shanghai Synchrotron Radiation Facility (SSRF). The data were collected in transmission mode or fluorescence mode using a Lytle detector while the corresponding reference samples were collected in transmission mode. The samples were grinded and uniformly daubed on the special adhesive tape.

The acquired EXAFS data were processed according to the standard procedures using the ATHENA module of Demeter software packages. The EXAFS spectra were obtained by subtracting the post-edge background from the overall absorption and then normalizing with respect to the edge-jump step. Subsequently, the $\chi(k)$ data of were Fourier transformed to real (R) space using a Hanning windows (dk=1.0 Å^{-1}) to separate the EXAFS contributions from different coordination shells. To obtain the quantitative structural parameters around central atoms, least-squares curve parameter fitting was performed using the ARTEMIS module of Demeter software packages. The following EXAFS equation was used:

$$\chi(k) = \sum_j \frac{N_j S_0^2 F_j(k)}{k R_j^2} \cdot exp[-2k^2\sigma_j^2] \cdot exp[\frac{-2R_j}{\lambda(k)}] \cdot sin[2kR_j + \phi_j(k)]$$

the theoretical scattering amplitudes, phase shifts and the photoelectron mean free path for all paths calculated. S_0^2 is the amplitude reduction factor, $F_j(k)$ is the effective curved-wave backscattering amplitude, N_j is the number of neighbors in the jth atomic shell, R_j is the distance between the X-ray absorbing central atom and the atoms in the jth atomic shell (backscatterer), λ is the mean free path in Å, $\phi_j(k)$ is the phase shift (including the phase shift for each shell and the total central atom phase shift), σ_j is the Debye-Waller parameter of the jth atomic shell (variation of distances around the average R_j). The functions $F_j(k)$, λ and $\phi_j(k)$ were calculated with the ab initio code FEFF9.

All fits were performed in the *R* space with *k*-weight of 2 while phase correction was also applied in the first coordination shell to make *R* value close to the physical interatomic distance between the absorber and shell scatterer. The coordination numbers of model samples were fixed as the nominal values. While the S_0^2, internal atomic distances *R*, Debye-Waller factor σ^2, and the edge-energy shift Δ were allowed to run freely.

3. Electrochemical measurements

The as-prepared Sn$_{SA}$-NC (or NC) was mixed with carbon black (super P) and polyvinylidene fluoride (PVDF) at the ratio of 8:1:1 and dispersed in N-methyl-2-pyrrolidone (NMP) for the slurry preparation. The obtained slurry was casted on

polypropylene separator (Celgard 2400), followed by vacuum dried at 40 °C for 18 h. The areal mass loading of the Sn_{SA}-NC@PP (or NC@PP) was ca. 0.3 mg cm^{-2}. The cathode electrodes were fabricated by mixing the S/C composites and PVDF at a ratio of 9:1 in NMP. The uniform slurry was bladed onto a carbon coated Al foil, followed by dried in vacuum at 40 °C for 18 h. The cathode electrodes were stamped into small round plates of 12.0 mm in diameter with the sulfur loading of 1 mg cm^{-2}. The coin-type CR2032 cells were assembled with the S/C electrode as the cathode, lithium foil as anode, and the modified PP as separator. 1 M lithium bis(trifluromethanesulfonyl)imide (LiTFSI) in 1,3-dioxolane and 1,2-dimethoxyethane (DOL/DME) solvent (1:1 by volume) containing 2 wt% LiNO$_3$ is used as electrolyte and the electrolyte/sulfur ratio was 20 (E/S = 20 μL mg^{-1}). Galvanostatic charge-discharge tests were performed on a LAND CT2001A Cell Test System with an electrochemical window of 1.7-2.8 V. The cells used for cycling tests at 0.5 C were first activated at 0.2 C for 3 cycles. The current density was based on the weight of sulfur (1 C = 1673 mA g^{-1}), and the specific capacities were calculated on the mass of sulfur. Cyclic voltammogram (CV) measurements were performed on a Solartron 1400 Cell Test System at various scan rates with a voltage range of 1.7-2.8 V. The cathode electrode of the cells used for the CV test adopts a recipe of S/MWCNT:PVDF = 9:1, while the others remain the same as before. The Li ion diffusion coefficient D_{Li+} was calculated according to Randles-Sevcik equation:[1]

$$I_p = (2.69 * 10^5)n^{1.5}SD_{Li+}^{0.5}C_{Li+}v^{0.5}$$

where I_p refers to peak current, n represents the charge transfer number, S is the area of the cathodes, C_{Li+} is the concentration of lithium ions in the electrolyte, and v is the scan rate. EIS analysis was measured in the frequency range from 100 kHz to 0.01 Hz with 10 mV amplitude at open circuit potential before cycle on a Solartron 1400 Cell Test System.

4. Polysulfides adsorption test

0.2 M Li$_2$S$_8$ solution, 0.5 M Li$_2$S$_6$ solution, 0.2 M Li$_2$S$_4$ solution was prepared by mixing sulfur and lithium sulfide with a mass ratio of 7:1, 5:1, 3:1 in a DOL/DME

(1:1, v/v) solvent with vigorous stirring for 48 h at 70 °C, respectively. 15 mg Sn_{SA}-NC and NC were added into 1 mL 5mmol Li_2S_8, Li_2S_6, Li_2S_4 solution for adsorption tests, respectively. Digital photos of the solutions were taken after aging for 6 h, which were also employed for UV-vis spectrum measurements.

5. Symmetric cell test

For the polysulfide redox conversion test, the electrodes were fabricated by mixing the Sn_{SA}-NC or NC and PVDF at a ratio of 3:1 in NMP. The uniform slurry was bladed onto Al foil coated carbon, followed by dried in vacuum at 60 °C for 18 h. Symmetric coin cells were assembled with 0.5 M Li_2S_6 electrolyte (40 μL) and two identical active electrodes as cathode and anode. The CV measurement of the symmetric cell was performed between -1 and 1 V.

6. Li$_2$S nucleation test

For the Li_2S nucleation measurement, the Sn_{SA}-NC, NC electrodes were fabricated by coating the slurry of the Sn_{SA}-NC or NC and PVDF at a ratio of 3:1 in NMP onto carbon paper. The Sn_{SA}-NC, NC and blank electrodes were assembled into half cells with lithium foils as counter electrodes. 0.2 M Li_2S_8 electrolyte (20 μL) and bare electrolyte (20 μL) were employed as catholyte and anolyte, respectively. For Li_2S nucleation, the assembled cells were discharged galvanostatically at 0.112 mA to 2.09 V and then discharged potentiostatically at 2.08 V until the current dropped below 10^{-5} A.

7. Theoretical calculations

All the calculations was performed within the framework of the density functional theory (DFT) as implemented in the Vienna Ab initio Software Package (VASP 5.4.4) code within the Perdew-Burke-Ernzerhof (PBE) generalized gradient approximation and the projected augmented wave (PAW) method.[2-5] The cutoff energy for the plane-wave basis set was set to 450 eV. The Brillouin zone of the surface unit cell was sampled by Monkhorst-Pack (MP) grids for catalyst structure optimizations.[6] A 5 × 3 supercell of the graphene surface was constructed to model the catalyst in this work. The Sn_{SA}-NC and NC catalysts were determined by 3 × 3 × 1 Monkhorst-Pack grid. The convergence criterion for the electronic self-consistent

iteration and force was set to 10^{-5} eV and 0.01 eV/Å, respectively. A vacuum layer of 15 Å was introduced to avoid interactions between periodic images.

The free energies of adsorbates and transition states at temperature T were estimated according to the harmonic approximation, and the entropy is evaluated using the following equation:

$$S(T) = k_B \sum_i^{harm\,DOF} \left[\frac{\varepsilon_i}{k_B T \left(e^{\varepsilon_i/k_B T} - 1 \right)} - \ln\left(1 - e^{-\varepsilon_i/k_B T}\right) \right]$$

where k_B is Boltzmann's constant and DOF is the number of harmonic energies (ε_i) used in the summation denoted as the degree of freedom, which is generally 3N, where N is the number of atoms in the adsorbates or transition states. Meanwhile, the free energies of gas phase species are corrected as:

$$G_g(T) = E_{elec} + E_{ZPE} + \int C_p dT - TS(T)$$

where C_p is the gas phase heat capacity as a function of temperature derived from Shomate equations and the corresponding parameters in the equations were obtained from NIST.

Transition states were located using the climbing image nudged elastic band (CI-NEB) method and each transition state was confirmed to have a single imaginary vibrational frequency along the reaction coordination.[7]

Supplementary Figures and Tables
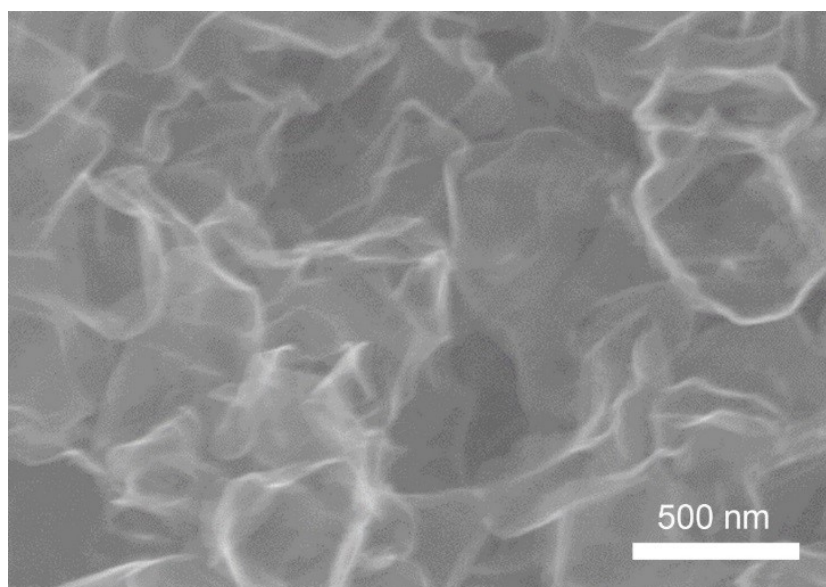
Figure S1. SEM image of Sn$_{SA}$-NC.
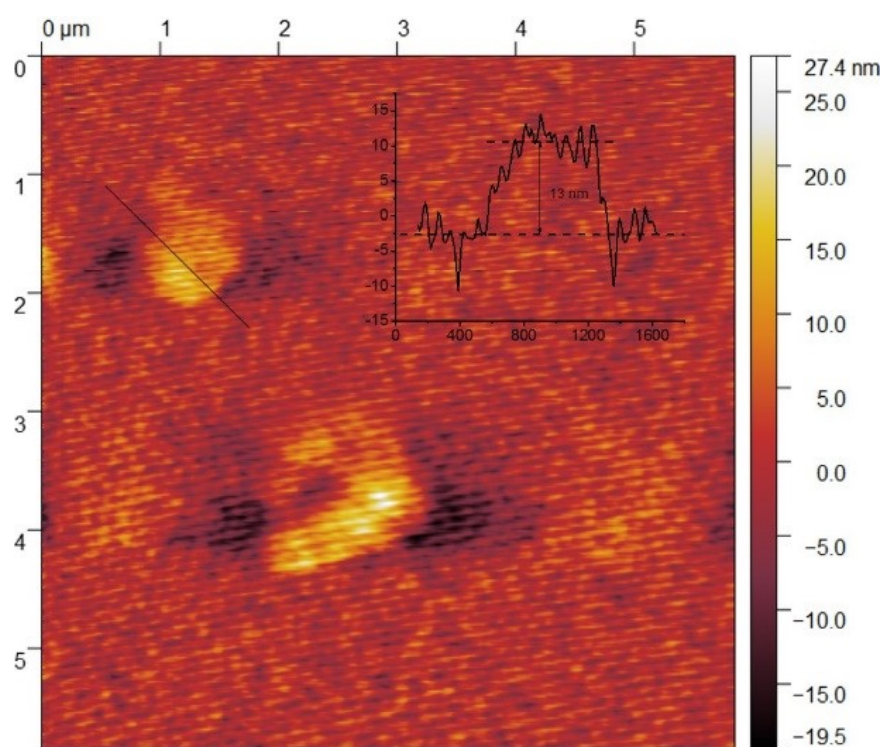
Figure S2. AFM image of Sn$_{SA}$-NC.
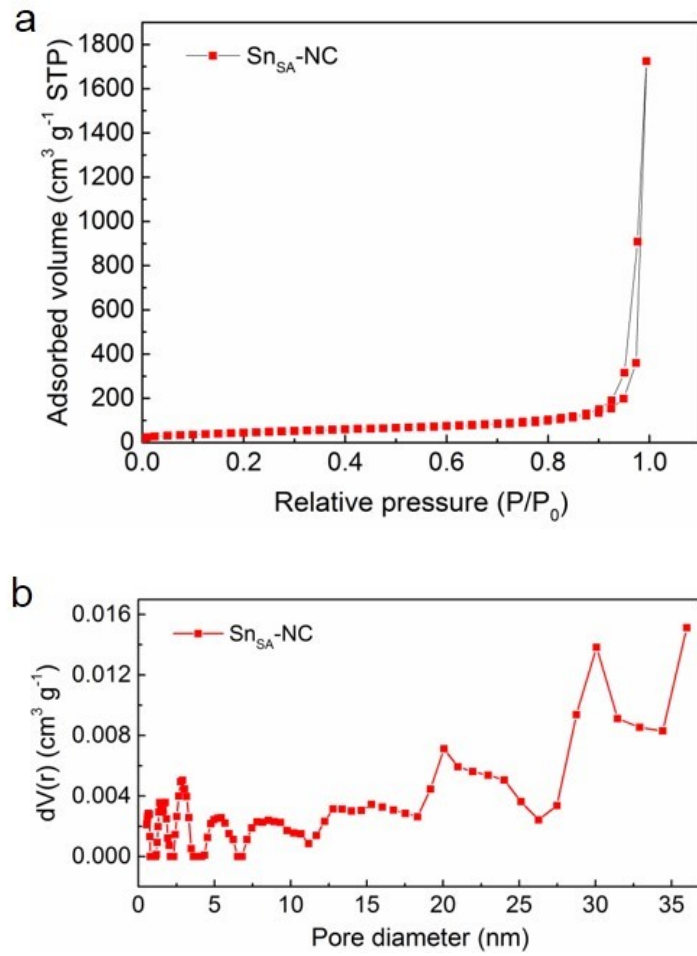
Figure S3. (a) N_2 adsorption/desorption isotherm and (b) pore size distribution of Sn_{SA}-NC.
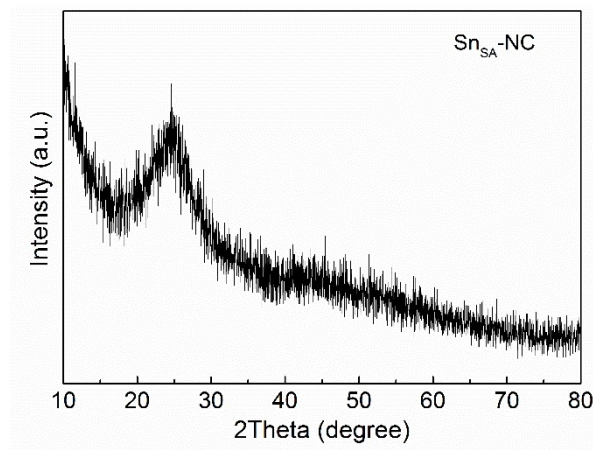
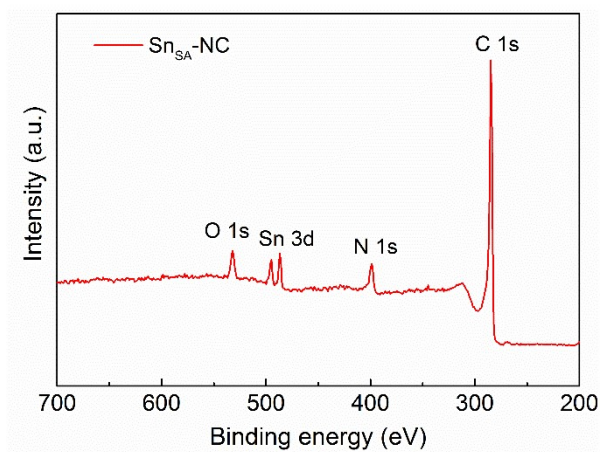**Figure S4.** XRD pattern of Sn_{SA}-NC.
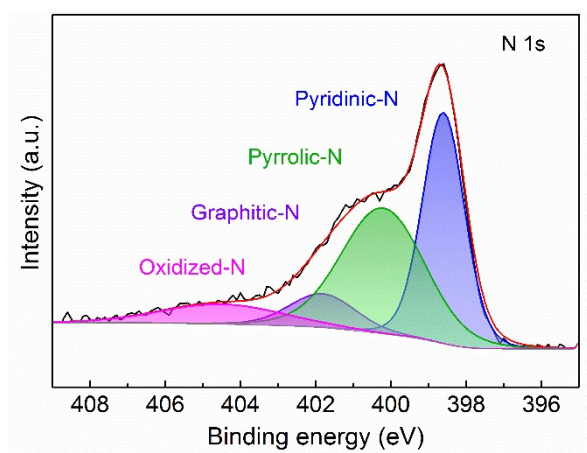
Figure S5. XPS survey spectrum of Sn_{SA}-NC.

Figure S6. XPS N 1s spectrum of NC.
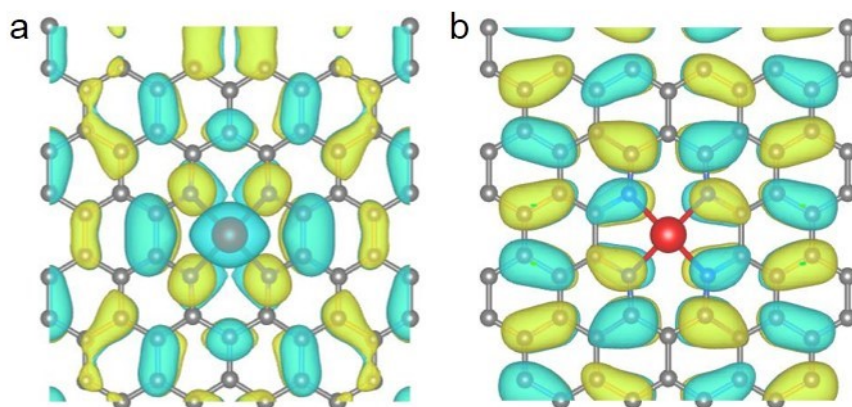
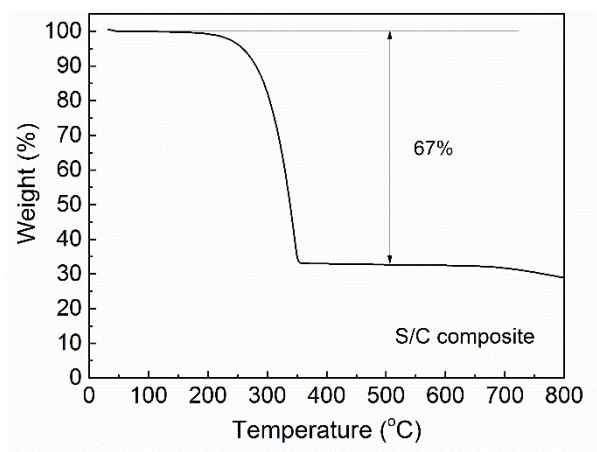**Figure S7.** (a) Valence band maximum (VBM) and (b) conduction band minimum (CBM) structures of $Sn-N_4$ model.

Figure S8. TGA curve of S/C composite in nitrogen.
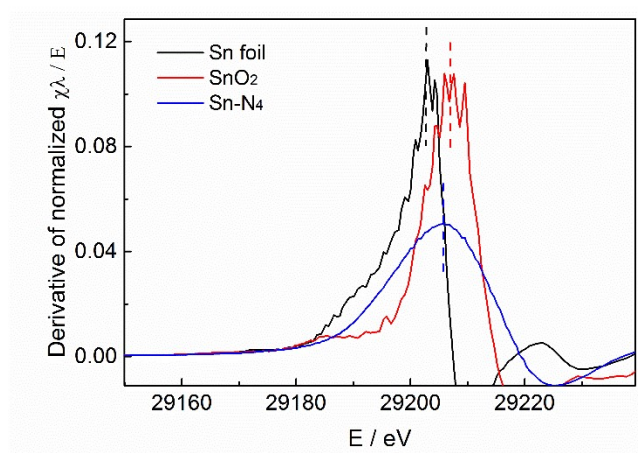
Figure S9. First-derivative XANES curves of Sn_{SA}-NC, Sn foil and SnO_2 at Sn K-edge.

Figure S10. The digital photograph of Li_2S_8 solutions after exposure to NC and Sn_{SA}-NC.

Figure S11. The digital photograph of Li$_2$S$_4$ solutions after exposure to NC and Sn$_{SA}$-NC.
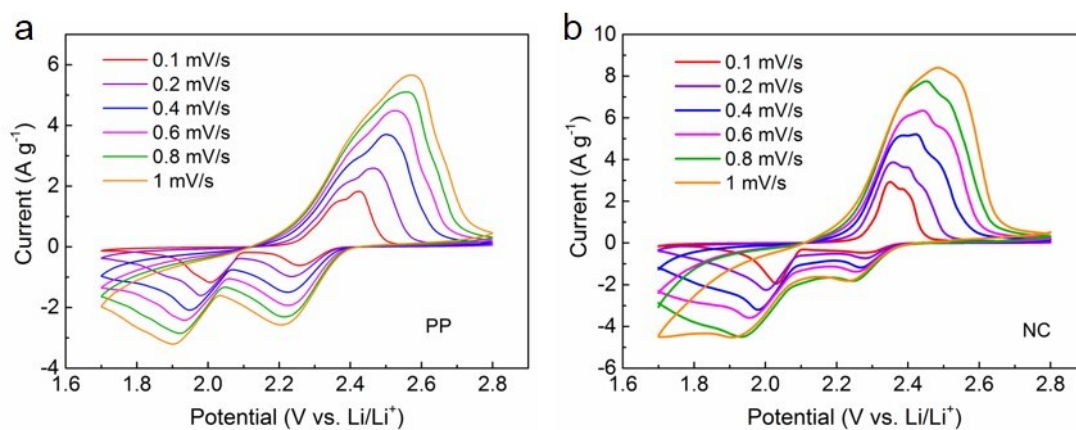
Figure S12. CV curves of the Li-S batteries with (a) unmodified PP, (b) the NC modified separator at different scan rates.
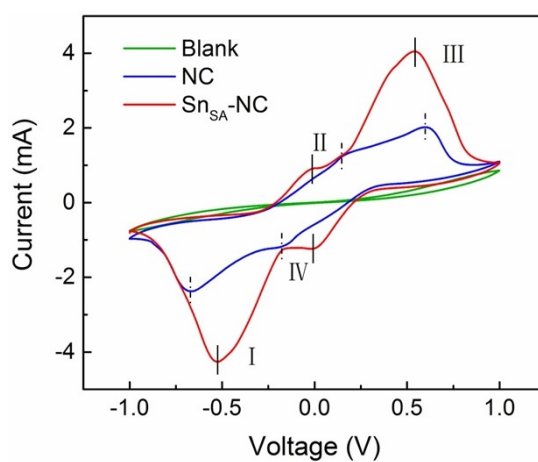
Figure S13. CV curves of the symmetric cells assembled using blank, NC, Sn$_{SA}$-NC electrodes at 1 mV/s.
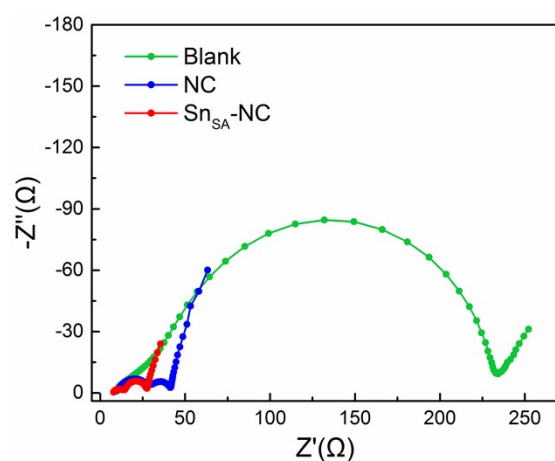
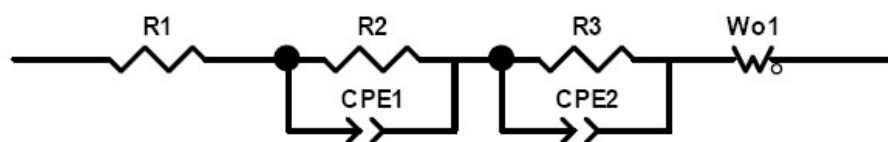**Figure S14.** EIS spectra of the symmetric cells assembled using blank, NC, Sn$_{SA}$-NC electrodes.

Figure S15. The corresponding equivalent circuit of EIS spectra of the symmetric cells assembled using blank, NC, Sn$_{SA}$-NC electrodes.
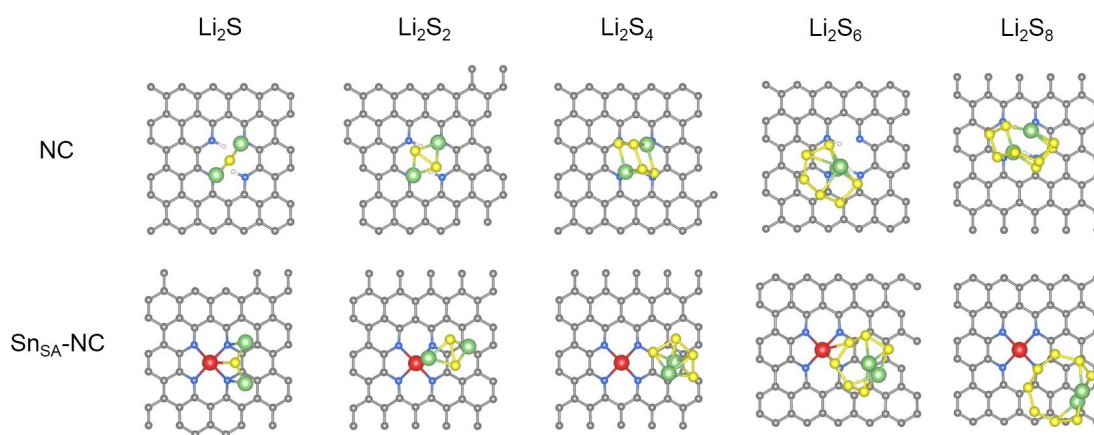

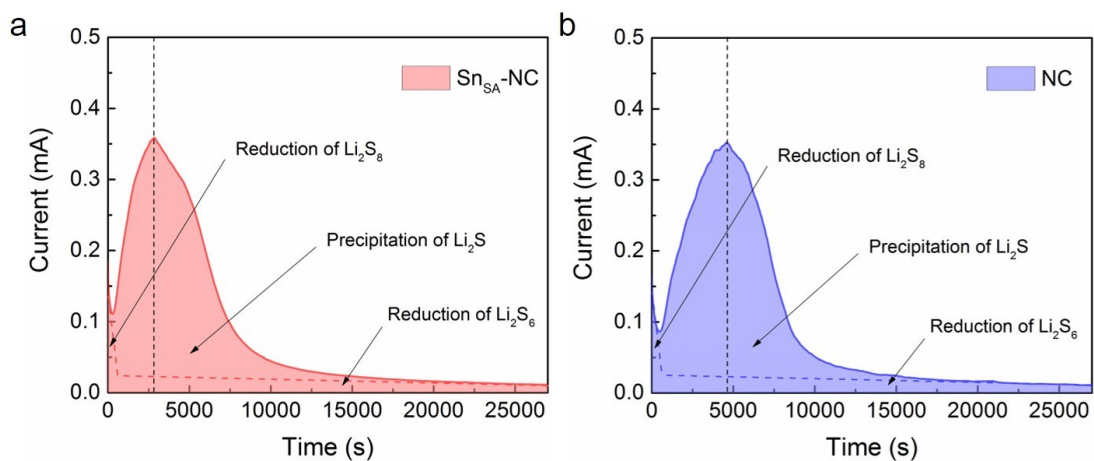**Figure S16.** Detailed adsorption atomic configuration for the polysulfides on NC, and Sn$_{SA}$-NC.

Figure S17. Potentiostatic discharge profiles at 2.08 V for the nucleation of Li_2S on the (a) Sn_{SA}-NC, (b) NC electrodes.

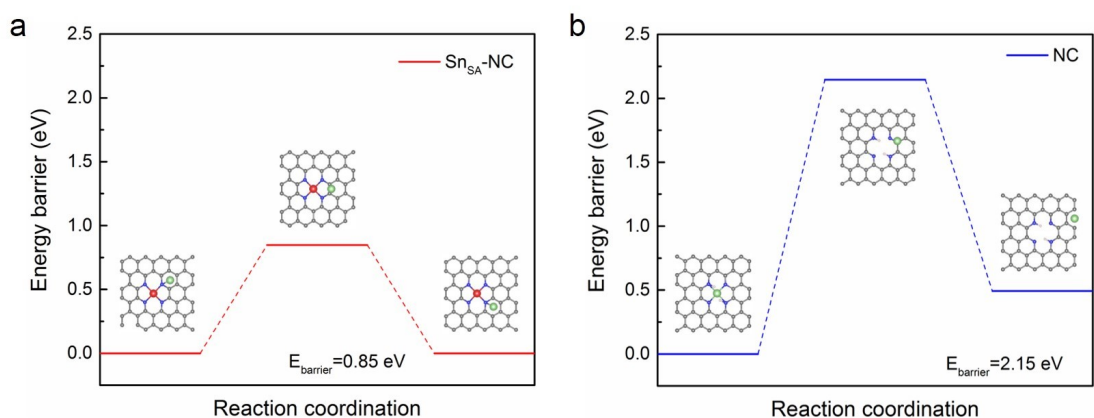**Figure S18.** Lithium ion diffusion barriers on (a) Sn_{SA}-NC and (b) NC. Insets demonstrate the detailed diffusion pathways of lithium atom on Sn_{SA}-NC and NC.
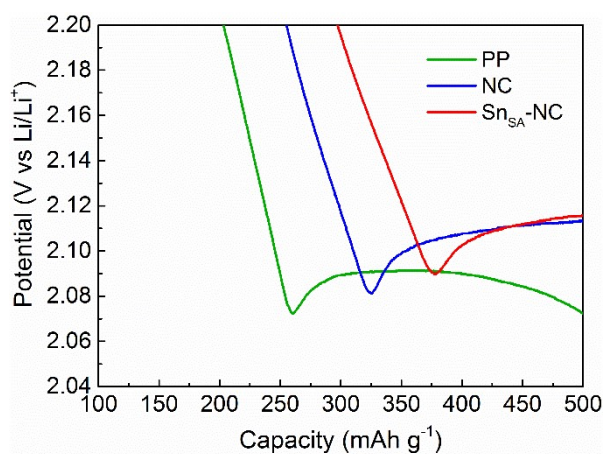

Figure S19. Enlarged discharge curve of the Li-S cells with unmodified PP, the NC,
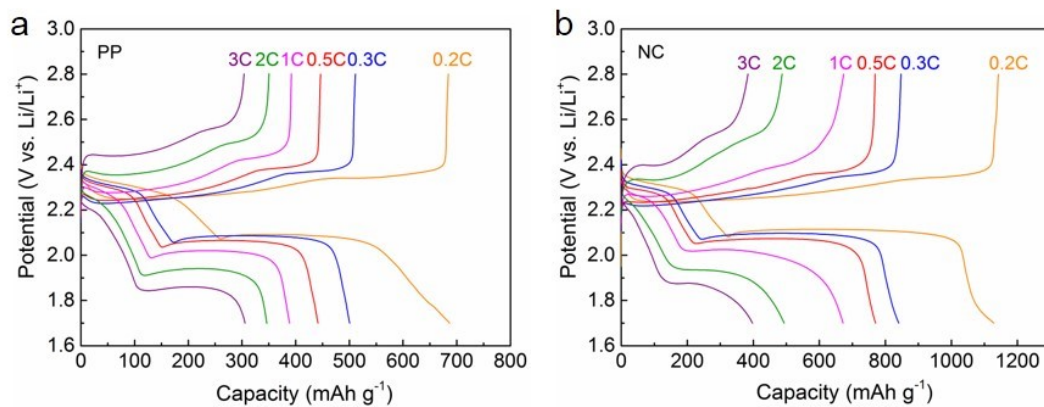
or Sn$_{SA}$-NC modified separators.

Figure S20. Charge-discharge voltage profiles of (a) PP and (b) NC modified separator at current rates of 0.2 C, 0.3 C, 0.5 C, 1 C, 2 C, and 3 C.
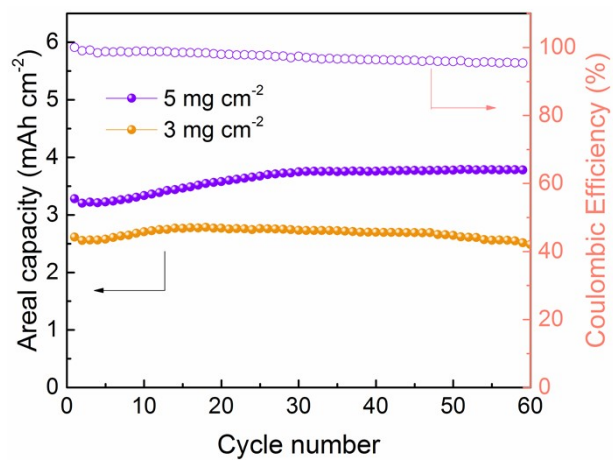

Figure S21. Cycling stability of Sn$_{SA}$-NC Li-S cells at a high sulfur loading of 3 mg cm^{-2} and 5 mg cm^{-2} at 0.2 C.
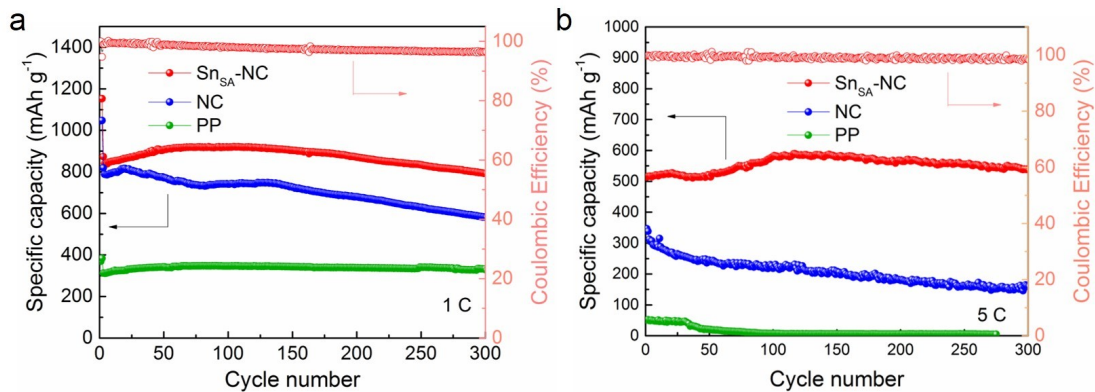
Figure S22. Cycling performance at (a) 1 C and (b) 5 C of PP, NC and Sn_{SA}-NC Li-S cells.

Table S1. Comparison of electrochemical performance of Li-S batteries employing single metal atom catalysts.

Single metal atom catalysts	Initial Capacity (mAh g^{-1})	High rate Capacity (mAh g^{-1})	Capacity decay rate per cycle	Ref.
Sn_{SA}-NC	1233/0.2 C	687@2 C	0.110%@0.5 C/300	This work
		603@3 C	0.031%@1 C/300	
SC-Co	1190/0.2 C	827@3 C	0.086%@0.5 C/300	[8]
SAV@NG	1100/0.2 C	605@3 C	0.073%@0.5 C/400	[9]
SACo@NG	1120/0.2 C	500@3 C	0.079%@0.5 C/400	[9]
FeNSC	1306/0.05 C	550@4 C	0.047%@1 C/1000	[10]
FeNC	1203/0.05 C	454@4 C	0.066%@1 C/1000	[10]
CNT@SACo	1443/0.1 C	641@2 C	0.064%@1 C/500	[11]
Fe-PNC	1139/0.1 C	275@2 C	0.200%@0.1 C/300	[12]
Co/PNC	1105/0.2 C	572@1 C	0.064%@1 C/300	[13]
Fe-N$_5$-C	1224/0.2 C	723@3 C	0.248%@0.2 C/100	[14]
Fe-N$_4$-C	1147/0.2 C	582@3 C	0.326%@0.2 C/100	[14]
FeSA-CN	1123/0.2 C	605@4 C	0.068%@0.5 C/200	[15]
C-C-N-Co	1160/0.1 C	582@5 C	0.269%@0.5 C/100	[16]
Co-N/G	1210/0.2 C	618@4 C	0.053%@1 C/500	[17]
Co-SAs/NC	1367/0.2 C	815@2 C	0.054%@1 C/500	[18]

References

1.	J.-Q. Huang, T.-Z. Zhuang, Q. Zhang, H.-J. Peng, C.-M. Chen and F. Wei, *ACS Nano*, 2015, **9**, 3002-3011.
2.	J. P. Perdew, K. Burke and M. Ernzerhof, *Phys Rev Lett*, 1996, **77**, 3865-3868.
3.	B. Hammer, L. B. Hansen and J. K. Nørskov, *Phys. Rev. B*, 1999, **59**, 7413-7421.
4.	P. E. Blöchl, *Phys. Rev. B*, 1994, **50**, 17953-17979.
5.	G. Kresse and D. Joubert, *Physical Review B*, 1999, **59**, 1758-1775.
6.	H. J. Monkhorst and J. D. Pack, *Physical Review B*, 1976, **13**, 5188-5192.
7.	G. Henkelman, B. P. Uberuaga and H. Jónsson, *The Journal of Chemical Physics*, 2000, **113**, 9901-9904.
8.	J. Xie, B. Q. Li, H. J. Peng, Y. W. Song, M. Zhao, X. Chen, Q. Zhang and J. Q. Huang, *Adv. Mater.*, 2019, **31**, 1903813.
9.	G. Zhou, S. Zhao, T. Wang, S.-Z. Yang, B. Johannessen, H. Chen, C. Liu, Y. Ye, Y. Wu, Y. Peng, C. Liu, S. P. Jiang, Q. Zhang and Y. Cui, *Nano Lett.*, 2020, **20**, 1252-1261.
10.	H. Zhao, B. Tian, C. Su and Y. Li, *ACS Appl. Mater. Interfaces*, 2021, **13**, 7171-7177.
11.	Q. Lin, B. Ding, S. Chen, P. Li, Z. Li, Y. Shi, H. Dou and X. Zhang, *ACS Appl. Energy Mater.*, 2020, **3**, 11206-11212.
12.	Z. Liu, L. Zhou, Q. Ge, R. Chen, M. Ni, W. Utetiwabo, X. Zhang and W. Yang, *ACS Appl. Mater. Interfaces*, 2018, **10**, 19311-19317.
13.	F. Zhang, S. Ji, H. Wang, H. Liang, X. Wang and R. Wang, *Small Methods*, 2021, 2100066.
14.	Y. Zhang, J. Liu, J. Wang, Y. Zhao, D. Luo, A. Yu, X. Wang and Z. Chen, *Angew. Chem. Int. Ed.*, 2021, **60**, 26622.
15.	C. Wang, H. Song, C. Yu, Z. Ullah, Z. Guan, R. Chu, Y. Zhang, L. Zhao, Q. Li and L. Liu, *J. Mater. Chem. A*, 2020, **8**, 3421-3430.
16.	Y. Li, P. Zhou, H. Li, T. Gao, L. Zhou, Y. Zhang, N. Xiao, Z. Xia, L. Wang, Q. Zhang, L. Gu and S. Guo, *Small Methods*, 2020, **4**, 1900701.
17.	Z. Du, X. Chen, W. Hu, C. Chuang, S. Xie, A. Hu, W. Yan, X. Kong, X. Wu, H. Ji and L.-J. Wan, *J. Am. Chem. Soc.*, 2019, **141**, 3977-3985.
18.	X. Zhou, R. Meng, N. Zhong, S. Yin, G. Ma and X. Liang, *Small Methods*, 2021, **5**, 2100571.